Rhodopsin-based voltage imaging tools for use in muscles and neurons of *Caenorhabditis elegans*

Negin Azimi Hashemi[a,b,1], Amelie C. F. Bergs[a,b,c,1], Christina Schüler[a,b], Anna Rebecca Scheiwe[a,b], Wagner Steuer Costa[a,b], Maximilian Bach[a,b], Jana F. Liewald[a,b], and Alexander Gottschalk[a,b,2]

[a]Buchmann Institute for Molecular Life Sciences, Goethe University, D-60438 Frankfurt, Germany; [b]Institute for Biophysical Chemistry, Goethe University, D-60438 Frankfurt, Germany; and [c]International Max Planck Research School in Structure and Function of Biological Membranes, Max Planck Institute of Biophysics, D-60438 Frankfurt, Germany

Edited by H. Robert Horvitz, Massachusetts Institute of Technology, Cambridge, MA, and approved July 10, 2019 (received for review February 11, 2019)

Genetically encoded voltage indicators (GEVIs) based on microbial rhodopsins utilize the voltage-sensitive fluorescence of all-*trans* retinal (ATR), while in electrochromic FRET (eFRET) sensors, donor fluorescence drops when the rhodopsin acts as depolarization-sensitive acceptor. In recent years, such tools have become widely used in mammalian cells but are less commonly used in invertebrate systems, mostly due to low fluorescence yields. We systematically assessed Arch(D95N), Archon, QuasAr, and the eFRET sensors MacQ-mCitrine and QuasAr-mOrange, in the nematode *Caenorhabditis elegans*. ATR-bearing rhodopsins reported on voltage changes in body wall muscles (BWMs), in the pharynx, the feeding organ [where Arch(D95N) showed approximately 128% ΔF/F increase per 100 mV], and in neurons, integrating circuit activity. ATR fluorescence is very dim, yet, using the retinal analog dimethylaminoretinal, it was boosted 250-fold. eFRET sensors provided sensitivities of 45 to 78% ΔF/F per 100 mV, induced by BWM action potentials, and in pharyngeal muscle, measured in simultaneous optical and sharp electrode recordings, MacQ-mCitrine showed approximately 20% ΔF/F per 100 mV. All sensors reported differences in muscle depolarization induced by a voltage-gated Ca^{2+}-channel mutant. Optogenetically evoked de- or hyperpolarization of motor neurons increased or eliminated action potential activity and caused a rise or drop in BWM sensor fluorescence. Finally, we analyzed voltage dynamics across the entire pharynx, showing uniform depolarization but compartmentalized repolarization of anterior and posterior parts. Our work establishes all-optical, noninvasive electrophysiology in live, intact *C. elegans*.

voltage imaging | all-optical electrophysiology | microbial rhodopsin | electrochromic FRET | neuromuscular

Activity of excitable cells like muscles and neurons is assessed by electrophysiology, Ca^{2+} or voltage imaging (1–7). While electrical measurements provide the highest sensitivity and temporal accuracy, imaging methods are much more versatile for applications in live animals and for recording multiple cells simultaneously. Genetically encoded Ca^{2+} indicators (GECIs) today cover most of the visible spectrum with comparably narrow spectral width, thus enabling multiplexing with other optical tools (8–10). Furthermore, GECIs were improved immensely since their first reporting in the late 1990s, to provide several thousandfold of fluorescence increases upon Ca^{2+}-binding (5). With differential kinetic properties, some GECIs enable detection of single action potentials (APs), and thus they are widely used in neuroscience. However, in many neuron types Ca^{2+} imaging fails to reflect spiking dynamics or subthreshold voltage fluctuations, or to assess high-frequency APs (11). Furthermore, Ca^{2+} measures neuronal activity indirectly, and neuronal depolarization is not always accompanied by a Ca^{2+} increase (12). Finally, GECIs are not well suited to detect hyperpolarization, as often Ca^{2+} does not decrease below basal cytosolic concentration. Thus, voltage imaging tools (GEVIs) are an important addition to the toolbox of sensors for excitable cell activity (11, 13–18).

The development of GEVIs lagged behind that of GECIs, and several different designs have been explored that couple voltage changes to fluorescence changes. These range from FRET sensors to circularly permuted GFP, similar as for GECIs (4, 5). However, such tools for a long time reached only a few percent in fluorescence change per 100 mV of membrane voltage change, making detection of single APs a challenge. More recently, microbial rhodopsins were found to exhibit a voltage-dependency of the fluorescence of their chromophore, retinal (17, 19). The fluorescence signal change was higher than for the other protein-based GEVIs (~20 to 40% per 100 mV), and was improved by mutagenesis (13, 18). However, the absolute fluorescence of the rhodopsins is very small, and in particular, the voltage sensitivity of the fluorescence, due to the nature of the process requiring more than 1 photon to be absorbed (20), becomes appreciable only at very high excitation light intensities. Thus, electrochromic FRET (eFRET) sensors were developed that couple fluorescence of a normal fluorescent protein (FP) to the rhodopsin. Upon depolarization, the latter acts as FRET acceptor, thus quenching the (much stronger) fluorescence of the FP, which

Significance

Neuronal and other excitable cell activity is characterized by alteration in membrane voltage, while intracellular Ca^{2+} levels and transmitter release are affected downstream of electrical activity. Thus, the most direct way of monitoring neuronal activity is by membrane voltage. Electrophysiology is demanding for multiple cells or cell ensembles and difficult to use in live animals, thus imaging methods are desirable. Yet, genetically encoded voltage indicators fell behind Ca^{2+} indicators until recently, when microbial rhodopsins and derivatives were introduced as genetically encoded voltage indicators. We evaluated rhodopsin tools for voltage imaging in muscles and neurons of *Caenorhabditis elegans*, a prime animal model in neuro- and cell biology, showing robust performance and the ability to characterize genetic mutants.

Author contributions: N.A.H., A.C.F.B., C.S., W.S.C., J.F.L., and A.G. designed research; N.A.H., A.C.F.B., C.S., A.R.S., M.B., and J.F.L. performed research; N.A.H., A.C.F.B., A.R.S., W.S.C., and M.B. contributed new reagents/analytic tools; N.A.H., A.C.F.B., C.S., A.R.S., W.S.C., J.F.L., and A.G. analyzed data; and A.G. wrote the paper.

The authors declare no conflict of interest.

This article is a PNAS Direct Submission.

This open access article is distributed under Creative Commons Attribution-NonCommercial-NoDerivatives License 4.0 (CC BY-NC-ND).

Data deposition: The plasmids used in this paper have been deposited in Addgene (https://www.addgene.org/search/advanced/?q=) via the following: pNH11 (pmyo-2::Arch(D95N)::2xMycTag) (Addgene ID 130275), pNH12 (pmyo-2::MacQ::mCitrine) (Addgene ID 130274), pNH13 (pmyo-2::QuasAr::mOrange) (Addgene ID 130273), pAB16 (pmyo-3::QuasAr) (Addgene ID 130272).

[1]N.A.H. and A.C.F.B. contributed equally to this work.

[2]To whom correspondence may be addressed. Email: A.Gottschalk@em.uni-frankfurt.de.

This article contains supporting information online at www.pnas.org/lookup/suppl/doi:10.1073/pnas.1902443116/-/DCSupplemental.

Published online August 1, 2019.

acts as a FRET donor (14, 16). Several variants of eFRET sensors were developed, which are composed of modified archaerhodopsins [Arch(D95N), QuasAr (18), Archon (13)], or other proton pumps like Mac (from *Leptoshaeria maculans*) or Ace2N, derived from the *Acetabularia* rhodopsin proton pump (14, 21, 22). Each of these proteins is coupled with specific linkers to fluorescent proteins—like mOrange, mCitrine, mNeon, or mRuby3—depending on the absorption of the respective rhodopsin, to achieve maximal FRET efficiency and imaging at different wavelengths. An alternative to improve voltage-dependent rhodopsin fluorescence may be to change the chemical properties of the chromophore. We previously used retinal analogs to reconstitute function of microbial rhodopsin optogenetic tools, altering their characteristics (23), and observed that some retinal analogs conferred higher fluorescence to the rhodopsin.

Here, we surveyed a range of microbial rhodopsin GEVIs in excitable cells of the nematode *Caenorhabditis elegans*, an important model system in physiology, molecular, cellular, and behavioral neurobiology. We show that eFRET sensors are robust tools allowing us to analyze voltage signals with little experimental effort, and that the retinal analog dimethylaminoretinal (DMAR) strongly improves absolute fluorescence. Direct voltage-dependent retinal fluorescence can be measured in the infrared under excitation at high intensity, both in muscles and in neurons, and membrane voltage can be adjusted concomitantly with rhodopsin tools for de- or hyperpolarization. Alterations in AP amplitude and duration were robustly detected in gain-of-function (g.o.f.) mutants of the L-type Ca^{2+} channel EGL-19 in a muscular pump, the pharynx, allowing correlation with the timing of pump events. Finally, GEVIs enabled us to visualize the spatiotemporal compartmentalization of voltage changes in this muscular structure.

Results

Arch(D95N) Equipped with ATR Shows Dim, Fluctuating Fluorescence in Muscle That Is Enhanced by DMAR. To explore the potential of analyzing muscle voltage changes via rhodopsin fluorescence, we expressed Arch(D95N) (17), QuasAr [an improved variant of Arch (18)], and Archon (13), a further evolved version, in body wall muscles (BWMs), or in pharyngeal muscles (PMs), and supplemented the animals with all-*trans* retinal (ATR). Under an epi-fluorescence microscope equipped with a 100 W HBO lamp for excitation and a sCMOS camera, very dim fluorescence was observable around 700 nm. Using a 637-nm laser and an EMCCD camera, fluorescence was more readily observable (Fig. 1 *A* and *B*). In comparison with Arch(D95N), QuasAr and Archon fluorescence was 2.4- and 2.1-fold more intense, respectively, showing 1.7-fold higher contrast over background fluorescence (in BWMs) (Fig. 1 *D* and *E*). In immobilized animals, BWM fluorescence intensity fluctuated in the range of 20 to 25% ΔF/F, likely representing voltage changes (*SI Appendix*, Fig. S1) that could correspond to APs, as recorded by patch clamp previously (24, 25).

When we supplemented animals with the retinal analog DMAR (23) (Fig. 1 *D*, *Inset*), we observed an approximately 250-fold higher absolute fluorescence (in PMs) (Fig. 1 *B* and *D*), and similarly, when we used retinal analog VI, fluorescence levels increased 81-fold [gain-corrected; note this was in Arch WT, in which analog VI does not mediate function, thus is not hyperpolarizing the cell; it could not be incorporated by Arch(D95N)]. This also led to higher contrast (138-fold and 44-fold for DMAR and analog VI, respectively) (Fig. 1*E*). Fluorescence yield of Arch(D95N) could also be increased by using 10× more ATR during animal cultivation, and 50× higher camera gain (Fig. 1 *B* and *D*). Increased fluorescence due to DMAR or increased ATR and gain was likewise observed in BWMs (Fig. 1*B*). Finally, we also expressed eFRET sensors, QuasAr-mOrange and MacQ-mCitrine,

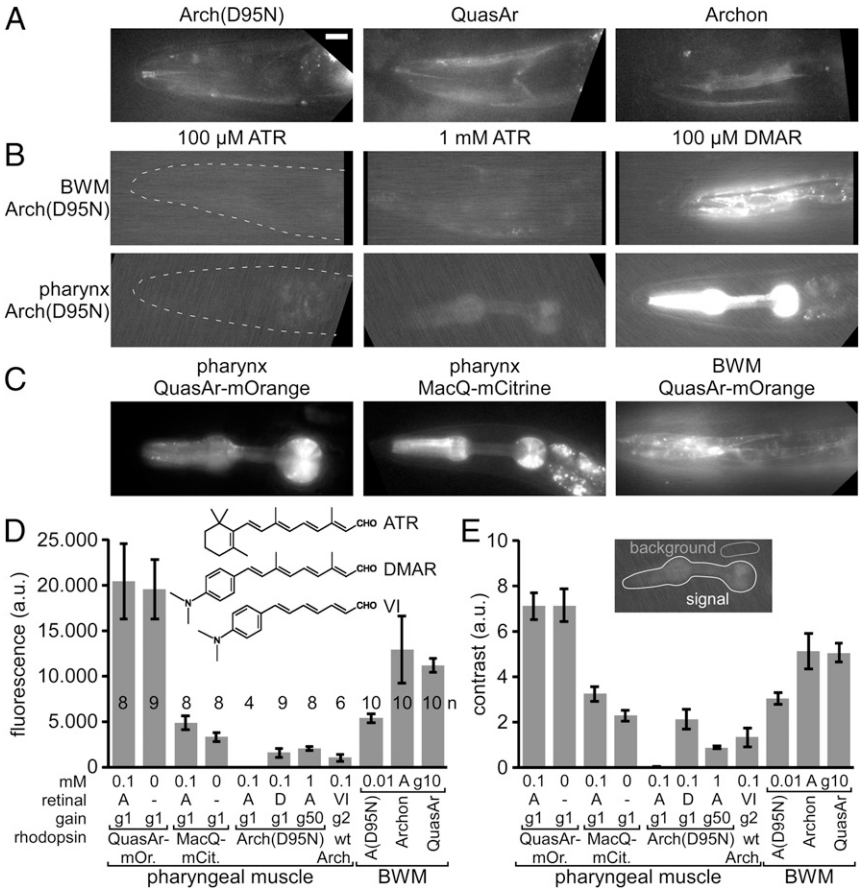

Fig. 1. Expression of rhodopsin voltage sensors in *C. elegans* muscle cells. (*A*) Expression and imaging of retinal fluorescence [Arch(D95N), QuasAr, Archon] in BWM cells in the head. (Scale bar, 10 µm. Scale for *B* and *C*, also 10 µm.) (*B*) Expression and imaging of Arch(D95N) in BWMs (*Upper*) and in PM (*Lower*), complemented with ATR (2 concentrations) and with the retinal analog DMAR (see *Inset* in *D* for chemical structures of ATR, DMAR and retinal analog VI). Dashed line indicates worm head. (*C*) Expression and imaging of eFRET voltage sensors (MacQ-mCitrine, QuasAr-mOrange) in PMs and BWMs. (*D* and *E*) Characteristics of basal fluorescence for the sensors expressed in PMs or BWMs, as indicated. Fluorescence intensity (*D*) as average gray values of an ROI enclosing the entire pharynx and contrast (*E*) as the ratio of signal over mean fluorescence of a control ROI were acquired (20-ms exposure) with different gain (indicated as "g" and a number). Rhodopsins were supplemented with ATR, DMAR, or analog VI ("A," "D," "VI"; concentrations in millimolars). Shown are means ± SEM. Number of animals imaged is indicated in *D*. In *A*–*C*, anterior is to the left.

in PMs or BWMs (Fig. 1*C*). Since for those, fluorescence of canonical FPs is observed, their absolute fluorescence was much higher than for any of the rhodopsin-only sensors [~3,000- and 800-fold higher fluorescence than Arch(D95N)-ATR, for QuasAr-mOrange and MacQ-mCitrine, respectively] (Fig. 1*D*). Moreover, their contrast level compared with background was 460- and 211-fold higher, respectively (Fig. 1*E*).

Intrinsic Activity in Muscle Is Accompanied by Fluorescence Changes of Rhodopsin GEVIs. To assess if the fluorescence of the sensors is also voltage-dependent, we observed it during intrinsic activity. For the pharynx, we immobilized animals such that pharyngeal pumping persists (i.e., treated with serotonin to mimic the presence of food). QuasAr-mOrange fluorescence changes were apparent upon PM contraction as a drop in intensity that was only observed when the protein was supplemented with ATR, thus yielding a functional eFRET acceptor (Fig. 2 *A* and *B* and Movie S1). The fluorescence of the terminal bulb (TB; "grinder" region) was further used to detect PM contractions.

For Arch(D95N) in BWMs, fluorescence fluctuations occurred at a rapid time scale (Fig. 2*C*), reminiscent of BWM APs appearing spontaneously in dissected animals, and which can be recorded by current-clamp electrophysiology (Fig. 2*E*). To explore whether fluorescence fluctuations occurred in response to muscular depolarization, we analyzed the muscle arms of QuasAr-expressing BWM cells in the head (Fig. 2*D* and Movie S2). Fluorescence fluctuated in a dorso-ventrally reciprocal fashion, as expected for the control of muscles during locomotion of the animal. As shown previously, such reciprocal activity is apparent in immobilized animals (26), even though at a slower pace than expected for freely moving animals. Fluctuations of 10 to 15% ΔF/F were found for all rhodopsin-based voltage sensors tested in BWMs [Arch(D95N), Archon, QuasAr] (Fig. 2 *F–H*, *SI Appendix*, Fig. S1, and Movies S3 and S4). These analyses were somewhat affected by movement: Animals were not anesthetized, thus photostimulation of cholinergic neurons led to muscle contraction and to a noisy baseline (*SI Appendix*, Fig. S1 *B*, *C*, *E*, and *J*). When we expressed and coactivated the hyperpolarizing anion-selective channelrhodopsin ACR2 (27, 28) in cholinergic motor neurons (MNs), fluorescence fluctuations in BWMs were absent and the baseline was less noisy, as inhibition of MNs paralyzes the animal (Fig. 2*I* and *SI Appendix*, Fig. S1 *F* and *J*). Thus, large fluctuations, most likely APs (see below), were evoked by presynaptic cholinergic MNs that depolarized BWM cells via acetylcholine (ACh) signaling, while noise was mostly due to movement.

QuasAr Enables Imaging of Electrical Activity in Neurons. To explore the possibility of imaging neuronal activity using QuasAr, we chose RIM neurons. These were previously shown to be active during locomotion, yet somewhat contradictory findings were reported (29–32): spontaneous reversals, or reversals evoked by mechanosensory neurons, reduced or increased RIM Ca^{2+} levels, which also show slow fluctuations; in addition, noxious stimuli evoked RIM hyperpolarization via glutamate signals. We thus attempted visualizing RIM voltage changes equivalent to these Ca^{2+} fluctuations, or in response to excitatory and inhibitory inputs. We expressed QuasAr in RIM neurons using the P*tdc-1* promoter. QuasAr::GFP could be readily observed in 2 neurons in the vicinity of the pharyngeal TB, which we identified as RIML and RIMR (Fig. 2*J*). When we imaged QuasAr fluorescence in immobilized animals, we observed phases lacking obvious activity (signals <1% ΔF/F) (Fig. 2*L*), that were interrupted by phases of activity: (*i*) the signal fluctuated rapidly for up to 4% ΔF/F, interrupted by (*ii*) short phases of increases or decreases of ΔF/F of up to 10%, and (*iii*) slow fluctuations either up- or downward of 5 to 15% (Fig. 2*K* and *SI Appendix*, Fig. S3 *A* and *B*). As a comparison, RIM Ca^{2+} signals showed similar slow fluctuations (*SI Appendix*, Fig. S3*A*), but no brief activity changes, likely as these electrical events are integrated to slower changes in Ca^{2+} concentration. When we measured (voltage-insensitive) RIM::GFP, we did not observe any rapid or long-lasting changes, and signal fluctuation was <1% ΔF/F (Fig. 2*K*). The brief pulses of de- or hyperpolarizing activity in RIM were of average amplitude of 8% ΔF/F, and lasted ~120 ms (*SI Appendix*, Fig. S2*C*). These events could correspond to inhibitory and excitatory inputs, evoking postsynaptic potentials. As a second example, we imaged cholinergic MNs. QuasAr expressed from the P*unc-17* promoter in retrovesicular ganglion MNs showed rapid fluctuations of ~4% ΔF/F, which were larger than the signals observed during inactive phases in RIM (Fig. 2*L* and *SI Appendix*, Fig. S3*B*). This indicated that these cells were active, but differed in their activity patterns from RIM. Cholinergic neurons have graded potentials, while RIM likely has a bistable membrane potential. These findings demonstrate that rhodopsin-based voltage imaging allows characterizing intrinsic neuronal and circuit activity, as previously shown in response to neuronal stimulation (13).

Optogenetic De- and Hyperpolarization of MNs Enables Calibration of Rhodopsin Voltage Signals in BWMs. To estimate how voltage-induced fluorescence changes compare with electrically measured voltages, we evoked BWM depolarization by optogenetic stimulation of cholinergic MNs. When recorded by current clamp, channelrhodopsin-2 (ChR2) stimulation evoked mean APs of 29.15 mV ($n = 8$) (Figs. 2*E* and 3 *A*, *B*, and *I*). We imaged BWM cell voltage using the 3 voltage sensors: Arch(D95N), QuasAr, and Archon. Imaging basal fluorescence signals with 637-nm laser excitation (Fig. 1*A*) (without actuator-mediated stimulation) revealed spontaneous brief increases of fluorescence of ~15% ΔF/F for QuasAr, and ~10% for Archon and for Arch(D95N) (Fig. 2 *F–H* and *SI Appendix*, Fig. S1). These lasted for ~50 to 100 ms, and were reminiscent of APs measured by electrophysiology in BWM cells (Fig. 2*E*). During prolonged recordings (25 s), QuasAr and Archon showed APs that cancelled out upon averaging, exhibiting only little change in baseline, while Arch(D95N) was photo bleaching (Fig. 2*C* and *SI Appendix*, Fig. S1 *A*, *D*, and *H*). When we used ChR2 stimulation of MNs, this led to increased ΔF/F signals, corresponding to depolarization: ~22.7% for QuasAr and Arch(D95N), and ~13.3% for Archon, for the first evoked peak (Fig. 3 *C–F*, and *I* and *SI Appendix*, Figs. S1 *B*, *C*, *E*, and *H–J*). Trains of APs could be observed that were overlaid on the overall increased fluorescence rise (*SI Appendix*, Fig. S1*J*). When averaged over the 5-s stimulus period, signals were ~21.4%, 14.6%, and 17.0% for QuasAr, Archon, and Arch(D95N), respectively. When we photo-hyperpolarized cholinergic MNs using ACR2, the fluorescence of QuasAr dropped by about 14.6%, and no AP-like spikes were observable (Figs. 2*I* and 3 *G–I* and *SI Appendix*, Fig. S1 *F–J*). Our measurements allow a rough calibration of the observed fluorescence voltage signals: ~78% ΔF/F per 100 mV for QuasAr and Arch(D95N), and approximately 46% for Archon, which resembles reported data [~45% ΔF/F per 100 mV for Arch(D95N) (17), QuasAr (18), and Archon (13)].

Arch(D95N) Shows Robust Fluorescence Increases in PMs. We assessed voltage-dependent changes in rhodopsin fluorescence in the pharynx in more detail. This muscular feeding pump exhibits APs and contractions. Arch(D95N), despite showing dim fluorescence, displayed strong fluorescence changes upon pharynx activity, on average ~122% ΔF/F (Fig. 4 *A* and *D* and Movie S5). The pharynx AP was previously reported to be between 80 and 115 mV (33–35), which we could confirm by our own sharp electrode recordings (Fig. 4*C*), on average 95.3 ± 3.6 mV (10 APs each from $n = 7$ animals). Thus, in PMs, 100-mV depolarization corresponds to ~128% fluorescence increase for Arch(D95N). This is larger than reported for Arch(D95N) or QuasAr in mammalian cells and neurons (17, 18), and also largely exceeds the fluorescence increase observed in BWMs upon excitation (Fig. 3 *C*, *D*, and *I*), for unknown reasons. The signal-to-noise ratio (SNR) was ~70 (Fig. 4*D*). Detecting Arch(D95N) fluorescence in BWMs requires a strong excitation laser (up to 1,800 mW/mm^2, 637 nm; in PMs, approximately one-tenth of this intensity was sufficient) and an EMCCD camera,

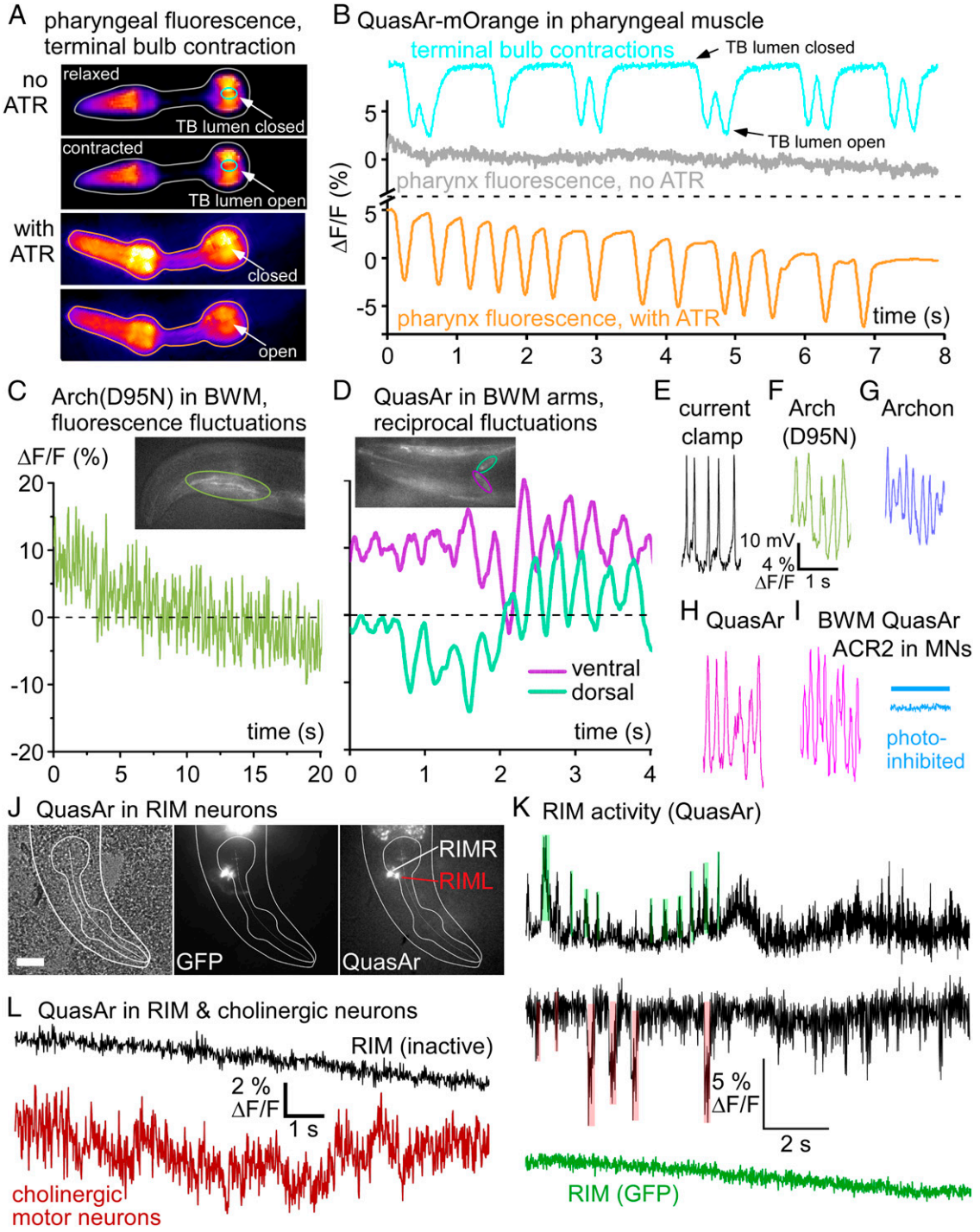

Fig. 2. Rhodopsin sensors detect intrinsic voltage changes in muscles and neurons. (*A*) Expression of QuasAr-mOrange in PMs, false-color representation of fluorescence intensity. *Upper* 2 images, animal raised without ATR; movie frames depict relaxed and contracted states. Time series of ROIs for fluorescence of the entire organ (gray) and for TB lumen (grinder region, cyan) are shown in *B*. *Lower* 2 images, animal supplemented with ATR (orange, voltage fluorescence ROI). Upon pharyngeal contraction fluorescence drops as TB lumen opens. (*B*) ΔF/F fluorescence time traces (acquired at 189 fps, 1-ms exposure) of ROIs indicated in *A*, in percent. Cyan graph: fluctuations of fluorescence signal due to opening and "darkening" of TB lumen, closed and open states. Without ATR, no change in fluorescence is observed despite pumping (gray trace; same movie as for TB contraction). Orange trace: Animal kept on ATR shows fluorescence drop upon PM depolarization; see also Movie S1. (*C*) Arch(D95N) fluorescence imaged in head BWM (ROI indicated in *Inset*; 158 fps, 2-ms exposure). (*D*) QuasAr imaging in BWM, dorsal, and ventral muscle arms in the nerve ring (ROIs indicated in turquoise and magenta), ΔF/F fluorescence shows dorso-ventral alternation. See also Movie S2. (*E*) APs recorded in dissected BWM, current clamp. (*F–H*) Fluorescence fluctuations of similar frequencies in BWM cells expressing Arch(D95N) (*F*), Archon (*G*), and QuasAr (*H*); each acquired at 158 fps, 2-ms exposure; see also Movies S3 and S4. (*I*) AP-like activity imaged in QuasAr-expressing BWM is stopped by ACR2-mediated photoinhibition of cholinergic motor neurons (blue trace, blue bar indicates illumination). (*J*) QuasAr::GFP expression in RIML and RIMR neurons. DIC (*Left*), GFP (*Center*), and QuasAr (*Right*) fluorescence in head region; outline of head and PM indicated. Scale bar, 20 μm. (*K*) QuasAr fluorescence fluctuations in RIM neurons (black traces), showing slow and fast inhibitory and excitatory events (shaded in red and green, respectively; for statistical analysis, see *SI Appendix*, Fig. S2*C*), while GFP (green trace) shows only photobleaching. (*L*) QuasAr fluorescence traces in RIM during inactive phase (black), and in cholinergic MNs (red). See also *SI Appendix*, Fig. S2.

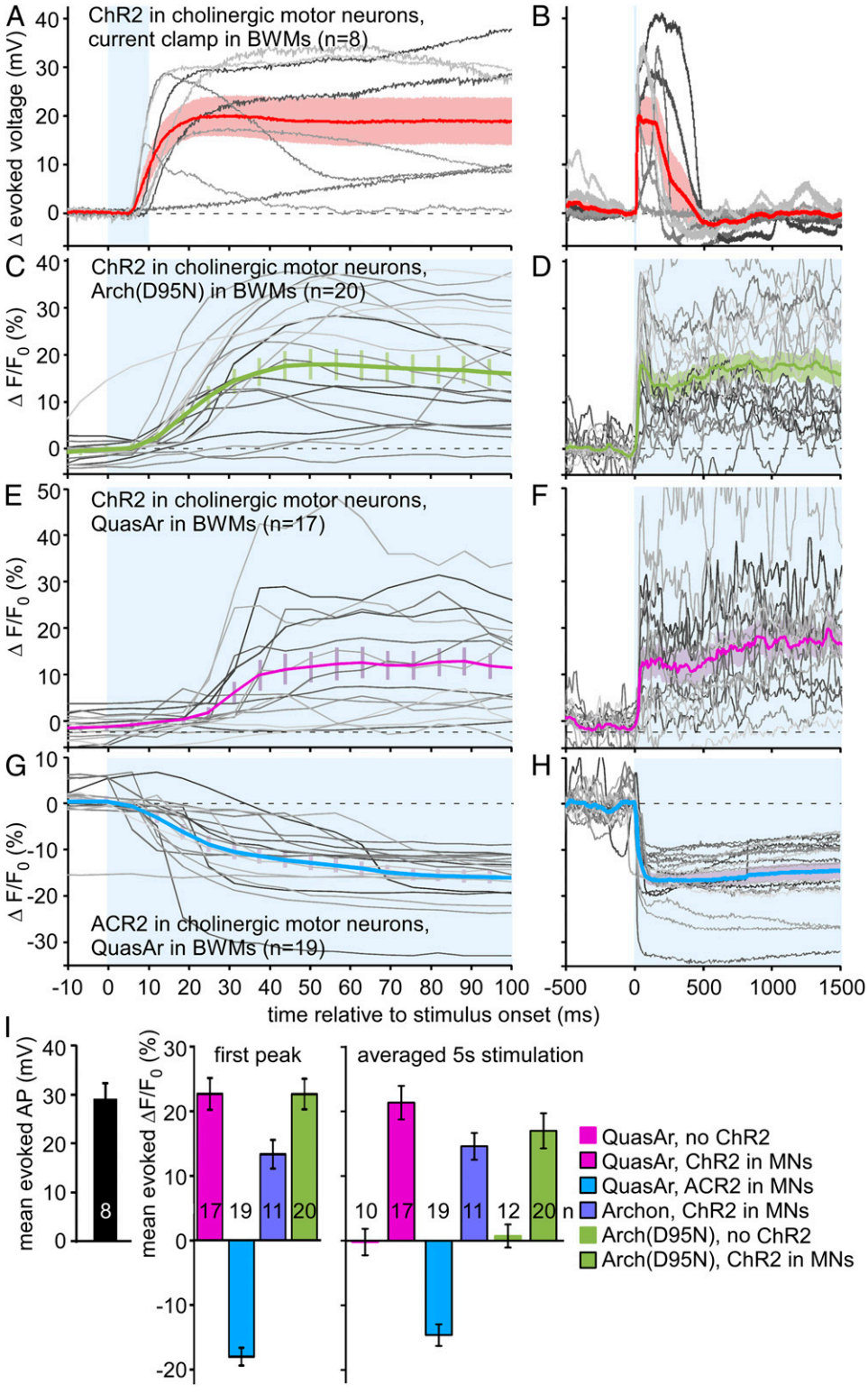

Fig. 3. Electrical and voltage-sensor signals in BWMs, induced by optogenetic manipulation of cholinergic MNs. (*A*) ChR2 mediated depolarization of cholinergic MNs (10-ms light pulse, indicated by blue shade) evokes APs in BWM cells, recorded under current clamp ($n = 8$ animals, single records in gray). Mean ± SEM voltage trace is shown in red and pink shade. (*B*) As in *A*, but extended time scale. (*C* and *D*) Arch(D95N) fluorescence voltage signals recorded in response to 5-s photodepolarization of cholinergic MNs by ChR2. Mean ± SEM and single records from indicated number of animals. (*E* and *F*) As in *C* and *D*, using QuasAr in BWMs. (*G* and *H*) As in *E* and *F*, but using ACR2 anion channelrhodopsin for hyperpolarization of cholinergic MNs. (*I*) Mean ± SEM analysis of the data shown in *A*–*H*, for electrically measured AP amplitudes, and for the first fluorescence peak (assuming first AP) or during the entire 5-s light stimulus, for indicated combinations of sensors, actuators, controls. Frame rate in *C*–*H*: 158 fps, 2-ms exposure. *n*, number of animals. See also *SI Appendix*, Fig. S1.

equipment not available in every laboratory. Thus, we assessed whether DMAR-supplemented Arch(D95N) would simplify voltage imaging. Fluorescence was largely increased (Fig. 1*D*) and could be visualized with a common sCMOS camera and excitation through an HBO lamp (30 mW/mm^2, 620 nm); however, this did not allow recording APs. Possibly, DMAR must also be strongly excited to report voltage: using laser excitation (~180 mW/mm^2, 637 nm), Arch(D95N)-DMAR showed activity-dependent fluorescence increases of ~27% (i.e., ~28.3%/100 mV), with an SNR of ~35 (Fig. 4 *A* and *D* and Movie S6). Signals were very uniform within a pump train in the same animal, but varied more between animals (*Discussion* and *SI Appendix*, Fig. S3 *A* and *B*). Thus, while the signal change per millivolt is ~5-fold lower for DMAR than for ATR, the increased detectability of the fluorescence makes this a valid alternative. We also tested analog VI in Arch WT; however, this retinal analog exhibited no voltage-dependence.

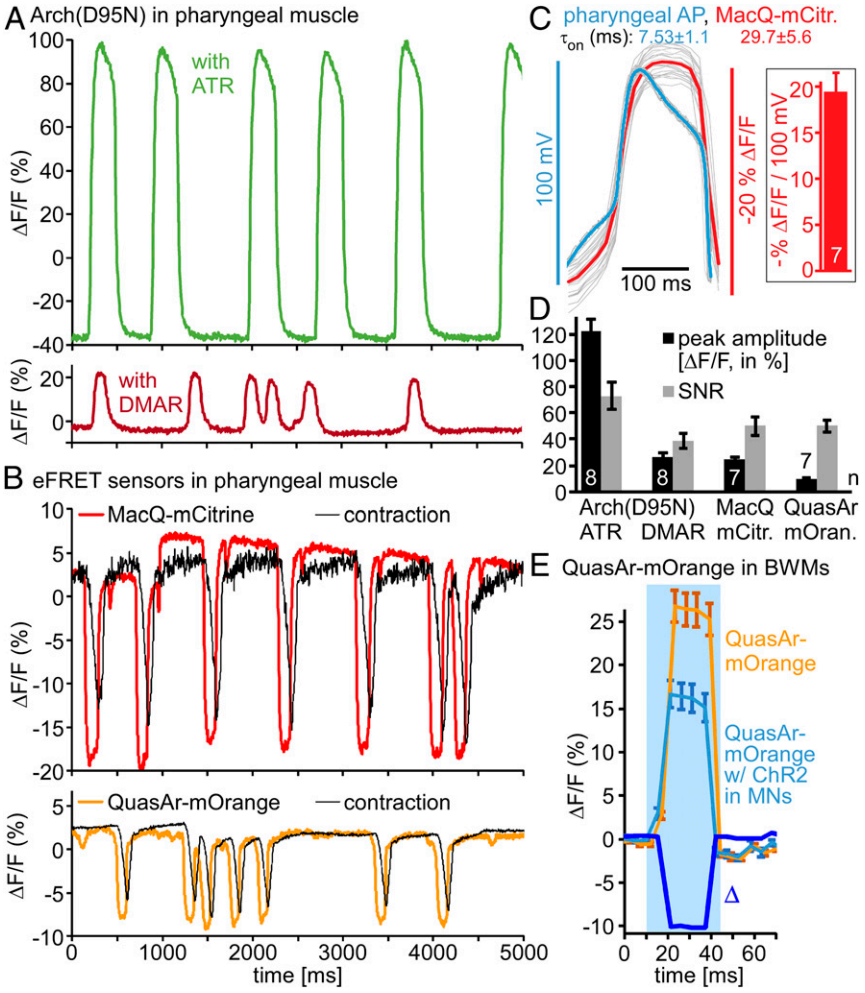

Fig. 4. Arch(D95N) and eFRET voltage-sensor signals quantified in PMs during pumping. (*A*) Arch(D95N) ΔF/F signals of PMs (entire organ) during pump trains, supplemented with ATR (above) or DMAR (below); see also Movies S5 and S6. (*B*) Pharyngeal APs, drop in fluorescence of eFRET sensors MacQ-mCitrine (*Upper*, red) (see also Movie S7) and QuasAr-mOrange (*Lower*, orange) (Movie S1). Corresponding TB contraction signal, black. (*C*, *Left*) Pharyngeal APs (overlay of 20 individual APs) and mean (blue), measured by sharp electrode recording (33), and concomitant ΔF/F signals measured from the same APs by MacQ-mCitrine (red, mean ΔF/F). (*Right*) Calibration ΔF/F per millivolt (each 10 APs from $n = 7$ animals). Also indicated are τ_{on} values for electrically and optically measured APs. (From ref. 33. Reprinted with permission from AAAS.) (*D*) Group data for sensors shown in *A* and *B*, mean ± SEM ΔF/F peak amplitudes, and SNR, defined as ratio of peak amplitude and SD of the noise (ΔF/F fluctuation between peaks). (*E*) QuasAr-mOrange signal in BWMs in response to photostimulation of ChR2 in cholinergic MNs (bright blue) or without ChR2 expression (orange), before and during a blue-light stimulus (blue shade). Both signals rise due to additional mOrange excitation. Difference graph (Δ, dark blue) shows drop in fluorescence upon ChR2-mediated stimulation. $n = 7$ to 8 animals, 3 to 15 APs each (or silent periods in between) were analyzed for *D*, and 12 to 13 animals in *E*. Frame rate in *A*, *B*, and *E*: 189 fps, 1-ms exposure.

eFRET Sensors Expressed in PMs Report on Voltage and Enable Concomitant Analysis of Muscle Contraction. As an alternative requiring no laser excitation, we analyzed the eFRET sensors QuasAr-mOrange and MacQ-mCitrine in PMs during pumping. A region of interest (ROI) encircling the entire pharynx was compared with an ROI outside the pharynx, but within the head of the animal (background). Fluorescence of both sensors was readily seen with standard epifluorescence microscope excitation intensities (HBO lamp or LEDs). MacQ-mCitrine and QuasAr-mOrange showed approximately −25 and approximately −10% reductions in the fluorescence upon pharyngeal pumping, respectively (Fig. 4*B*, *SI Appendix*, Fig. S3 *C–F*, and Movies S1 and S7). SNR was comparable for both sensors (∼50) (Fig. 4*D*). Thus, despite lower overall fluorescence (Fig. 1*D*), MacQ-mCitrine is the more sensitive voltage reporter. Signals for both sensors were quite uniform in the same animal, while mean signal traces between animals varied (*SI Appendix*, Fig. S3 *C–F*). For rigorous calibration of MacQ-mCitrine fluorescence signals, we concomitantly recorded membrane voltage by sharp electrodes from the same dissected pharynxes. Measured APs were 95.3 ± 3.6 mV (10 APs each from $n = 7$ animals) (Fig. 4*C* and *SI Appendix*, Fig. S3 *G* and *H*), and the corresponding signals of MacQ-mCitrine were 19.49 ± 2.03% ΔF/F per 100 mV (Fig. 4*C*). Optically determined signals increased more slowly than the electrically determined voltages (time constants, electrical: τ_{on} = 7.53 ± 1.1 ms, τ_{off} = 5.02 ± 0.7 ms; ΔF/F: τ_{on} = 29.7 ± 5.6 ms, τ_{off} = 38.7 ± 9.4 ms). The protein-based measurement is thus ∼4× "slower," which should be kept in mind when analyzing very fast events. QuasAr-mOrange signals corresponded to ∼10.5% ΔF/F per 100 mV in PMs. In BWMs, we "calibrated" QuasAr-mOrange signals following ChR2 stimulation in MNs, by comparing this to similarly illuminated animals lacking ChR2 (Fig. 4*E*): although mOrange excitation causes some ChR2 stimulation, a blue-light pulse resulted in different fluorescence increases in the 2 strains (∼10% smaller for animals expressing ChR2). As photoevoked APs are 29 mV (Fig. 3*I*), this amounts to approximately −34% ΔF/F per 100 mV. Thus, QuasAr-mOrange appears to be more sensitive in BWMs than in PMs.

Analyzing a small ROI enclosing the pharyngeal TB grinder region allowed deriving the opening of the pharynx from the fluorescence signal (Figs. 2 *A* and *B* and 4*B*). Thus, we could correlate depolarization and contraction of the muscle. We wrote scripts to systematically analyze the measured fluorescence traces. These involved automatic detection of relevant events, aligning, synchronizing, and averaging. Then, parameters could be derived such as amplitude, area under the peak (corresponding to charge transfer), AP- and pump-duration (both defined as rise from and return to the baseline, or by using the full-width at half-maximum), delay of pump versus voltage, or rise and drop of the voltage as τ_{on} and τ_{off} values (Fig. 5*A*). Signals could be analyzed and compared for Arch(D95N) equipped with ATR and DMAR, MacQ-mCitrine, and QuasAr-mOrange (Fig. 5 *B–H*) (8 to 15 animals with 2 to 10 APs, each): pumps could not be deduced for Arch(D95N)-ATR as the basal fluorescence was too dim to detect TB opening. A comparison between signals observed by the tested sensor-retinal combinations showed, as deduced from manual analysis, different amplitudes of the pharyngeal AP [132, 22.6, −23.5, and −11.6% $\Delta F/F_0$ for Arch(D95N)-ATR, Arch(D95N)-DMAR, MacQ-mCitrine, and QuasAr-mOrange, respectively], while the duration of the AP was

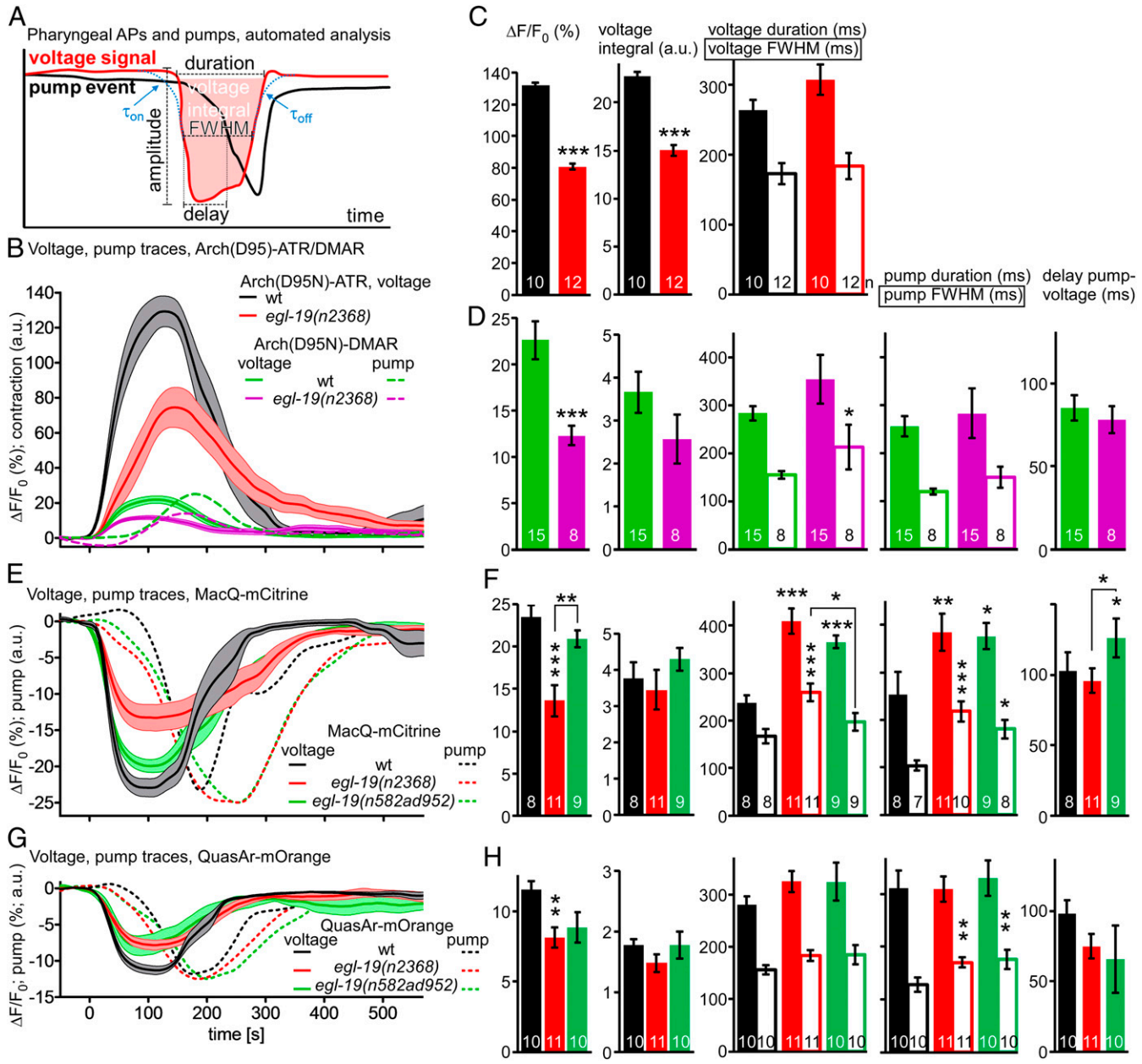

Fig. 5. Pharyngeal AP and pump parameters quantified by automated analysis in WT and L-type VGCC g.o.f. mutants. (*A*) Automated analysis of pharyngeal AP parameters and corresponding TB contraction, determined after extraction and alignment of AP and pump events from fluorescence traces (see *Materials and Methods* for details). (*B*) Mean ± SEM data obtained using Arch(D95N) equipped with ATR and DMAR, in WT and in *egl-19(n2368)* mutants. (*C* and *D*) Mean ± SEM of AP and pump parameters deduced from data in *B*. (*E*–*H*) Mean ± SEM data and parameters deduced from MacQ-mCitrine (*E* and *F*) or QuasAr-mOrange recordings (*G* and *H*). Frame rate in *B*, *E*, and *G*: 189 fps, 1-ms exposure. Data in *C*, *D*, *F*, and *H* were statistically analyzed by ANOVA, Bonferroni correction. ***$P \leq 0.001$, **$P \leq 0.01$, *$P \leq 0.05$.

very similar (264, 283, 238, and 281 ms, respectively; no significant difference, n.s.). For Arch(D95N)-DMAR, MacQ-mCitrine, and QuasAr-mOrange, we could also compare other parameters among the sensors: the pump duration was 255, 264, and 304 ms, respectively (n.s.); the delay from voltage rise to pump onset was 85, 103, and 98 ms, respectively (n.s.); voltage signal τ_{on} (~15 ms; i.e., smaller than measured in Fig. 4*C*, likely due to the cut worm preparation versus intact animals) and τ_{off} (~35 ms), as well as pump rise [erroneous for Arch(D95N), 23 to 39 ms for the eFRET sensors] and decay time constants (19 to 39 ms) (*SI Appendix*, Fig. S4) were not significantly different between sensors. This shows tight coupling of pharyngeal voltage and contraction kinetics, observable with each sensor, and allows correlating these events. It should also allow characterizing aberrations in mutants affecting PM physiology, in ways not possible by electrophysiology, as muscle movement makes precise intracellular recordings demanding or even precludes them.

"Gain-of-Function" Mutations in L-Type Channels Prolong Pump Duration but Reduce Voltage Increases. We used the voltage sensors to quantitatively compare mutants affecting the L-type voltage-gated Ca^{2+} channel (VGCC) EGL-19. This channel carries currents shaping the plateau phase of the pharyngeal AP (36, 37). Loss-of-function mutants are lethal; however, several g.o.f. alleles were isolated and, due to EGL-19's additional

function in BWMs, characterized as affecting muscle tone. We analyzed 2 g.o.f. alleles, *n2368* and *n582ad952*. These affect amino acids close to the pore domain of the second VGCC module (*n2368* → G365R), or a double mutation in the pore of the first and the voltage sensor of the third module (*n582ad952* → S372L, R899H). We compared 8 to 15 animals per genotype, 2 to 10 APs per animal. Imaging PM activity with Arch(D95N)-ATR or -DMAR or the 2 eFRET voltage sensors showed a significantly reduced AP amplitude for *n2368* (to 52 to 65% of the WT) (Fig. 5 *B–H*), and a reduced signal (n.s.) for *n582ad952*. For MacQ-mCitrine, both alleles showed significantly prolonged AP and pump durations (Fig. 5 *E* and *F* [pump duration was also increased for QuasAr-mOrange] and Fig. 5 *G* and *H*). Thus, g.o.f. describes the effect of these alleles on PM contraction properties (i.e., prolonged pump). Respective the AP [which in BWMs is similarly reduced in amplitude, although also prolonged (24, 25)], these alleles are hypomorphic rather than g.o.f. The dihydropyridine analog nemadipine A (NemA) is a potent inhibitor/accelerates desensitization of EGL-19 (38, 39). We analyzed the influence of NemA on voltage-dependent PM fluorescence signals, compared with animals incubated in just the DMSO-containing vehicle (*SI Appendix*, Fig. S5). As expected, NemA decreased WT voltage signals, and essentially restored the *egl-19* g.o.f. alleles to DMSO-control levels in WT. This was true for all sensors tested [Arch(D95N)-DMAR, QuasAr-mOrange, and MacQ-mCitrine], although to different degrees. In sum, voltage imaging is a valuable method for characterization of ion channels, and more easily applied than electrophysiology.

Imaging Spatially Compartmentalized Voltage Signals in the Pharynx. Electrophysiology is difficult in electrically coupled cell systems, thus precluding analysis of compartmentalization of cell ensembles. This is expected to be the case for the pharynx, where anterior and posterior portions act differently, as implied by the different events visible in electropharyngeograms (EPGs i.e., extracellular recordings of pharyngeal electrical activity) (40–42). EPGs are current recordings with a complex, yet stereotypic structure (Fig. 6*C*), corresponding to PM depolarization and repolarization events, including currents due to inhibitory neurons that terminate the pharyngeal AP. These different events are not spatially resolvable by EPG recordings, and cannot be addressed by simultaneous sharp electrode recordings from different sections of the pharynx (33–36, 43). We thus assessed compartmentalized PM activity by voltage imaging. A MacQ-mCitrine recording of a pump train with uniform single events (Movie S7) was processed to represent changes in voltage, rather than absolute signals. We calculated difference movies, and after aligning and averaging, we could clearly observe depolarization and repolarization events (Fig. 6*A* and Movie S8). Spatiotemporal differences in voltage-change rate along the longitudinal axis of the pharynx were obvious (Fig. 6 *A* and *B*). All PMs synchronously depolarized, while repolarization, following approximately 144 ms later, occurred first in the anterior PMs (the corpus), and 50 ms later in the isthmus and TB. A small section connecting the corpus and isthmus showed additional depolarization between the 2 repolarization events (161 ms). This region could match the connection between pm5 and pm4 muscle cells, where multiple inputs from pharyngeal neurons occur that could underlie the minor signal. It will be interesting to visualize this region in more detail, ideally with markers for pharyngeal neuron cell types. The EPG measures currents from the extracellular medium into the PMs and thus represents changes in muscle polarization. We wondered if mean voltage-difference events, averaged across the whole pharynx, would correspond to the EPG. We simultaneously recorded EPGs and optical eFRET signals of MacQ-mCitrine. Optical signals only occurred when ATR was present, and matched the electrical recordings very well (*SI Appendix*, Fig. S6). When we calculated the inverse mean signal change of the entire pharynx, it fitted the EPG recording precisely (Fig. 6*C*). A single depolarization spike (corresponding to "E" or "E2") was followed by 2 repolarization spikes, corresponding to the anterior and posterior parts of the pharynx ("R1" and "R2") (40, 42–45). In sum, optical measurements match EPGs, yet outperform them with respect to spatial information.

Discussion

We surveyed microbial rhodopsin-based voltage sensors in different muscles and neurons of *C. elegans*. These include the rhodopsins Arch(D95N) (equipped with ATR and the retinal analog DMAR), QuasAr, and Archon, as well as the eFRET sensors MacQ-mCitrine and QuasAr-mOrange. We show that all of them detect APs with robust fluorescence changes of up to 128% per 100 mV in the pharynx, and 78% in BWMs. These values were larger than previously reported for other organisms. This may result from different lipid compositions of *C. elegans* membranes, beneficially influencing Arch' properties. Making these high $\Delta F/F_0$ values accessible, however, required high-power laser excitation (up to 1,800 mW/mm^2 637-nm light), achievable only in a small field-of-view, as well as an EMCCD camera, to enable recording at a high frame rate despite the low absolute fluorescence. Addition of ATR to the culture medium caused increased background fluorescence upon blue-light stimulation, thus low concentrations of ATR are recommended. Lower excitation light intensities (180 mW/mm^2) were sufficient when using DMAR as an alternative to ATR. DMAR strongly boosted the absolute fluorescence levels, yet reduced the fluorescence change per voltage change by a factor of 5. Possibly, a similar branched photocycle as in Arch(D95N)-ATR (20) is present with DMAR, requiring more than 1 photon to be absorbed. However, it was feasible to use this sensor/retinal analog combination to robustly measure parameters of pharyngeal pumping that were similar to those measured with the eFRET sensors, and to compare VGCC g.o.f. mutants to WT.

Despite 75% lower absolute fluorescence intensity, the MacQ-mCitrine eFRET sensor showed approximately 3-fold higher $\Delta F/F$ than QuasAr-mOrange. Parameters of pharyngeal APs and pumping were similar for all sensors, emphasizing that they did not alter the properties of the pharynx, and our sharp electrode recordings did not reveal PM properties different from previous reports (33–35). Electrophysiological measurements are demanding and do not allow concomitant analysis of muscular movement and contraction parameters, while our imaging approach does. Since the parameters we measured in WT and *egl-19* g.o.f. alleles were not altered by the 3 sensors, we expect that other mutations affecting pharyngeal physiology and pumping will also be accessible using the methods described here. Furthermore, we showed that NemA, a VGCC blocker, similarly affected—actually restored—pharyngeal AP characteristics in *egl-19* g.o.f. mutants, as shown earlier by electrophysiology (38). The signals we determined for pharyngeal voltage fluorescence fluctuations were quite comparable in pump trains of single animals, but differed across animals. This may be due to the differences in immobilization of each individual and might be improved by more reproducible immobilization conditions (e.g., in microfluidic devices).

Our imaging approach allows following fluorescence fluctuations in a spatiotemporally defined manner across an ensemble of electrically coupled cells. This confirmed earlier assumptions made from EPG recordings (i.e., that TB repolarization is delayed relative to corpus repolarization). Due to movement, this cannot be simultaneously measured by sharp electrodes in the 2 parts of the pharynx, emphasizing that optical measurements provide new possibilities. We observed not only the functional electrical compartmentalization of the 2 pharyngeal halves but also observed smaller subcompartments at their interface, with potentially distinct electrical activities during distinct phases of excitation-repolarization. This could be further assessed, for example, in gap junction mutants or cell-specific knockdown animals. Evaluating voltage change rates across the

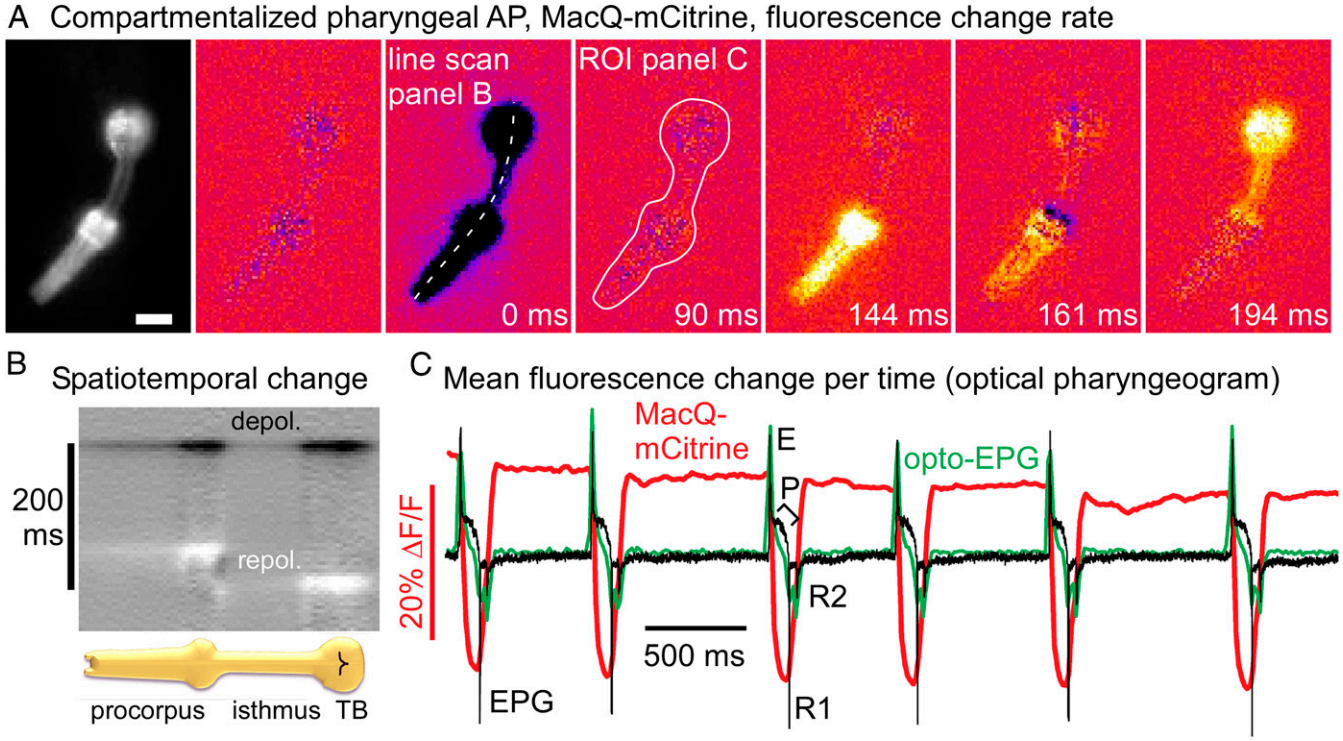

Fig. 6. Pharyngeal AP repolarization occurs in a spatiotemporally compartmentalized fashion. (*A*) A MacQ-mCitrine fluorescence movie (191 fps, 1-ms exposure) of a pharyngeal pump train was analyzed by measuring fluorescence differences from frame to frame and averaging 12 events, aligned to peak depolarization rate (0 ms, as indicated). (Scale bar, 20 μm.) Dark and bright colors represent high rates of depolarization and repolarization, respectively (Movie S8). Linear ROI along axis of the pharynx allows generating a kymograph (*B*) for analysis of spatiotemporal development of voltage; synchronous depolarization, consecutive repolarization of corpus and TB. An ROI around the entire pharynx allows generating an "optical EPG" (*C*) by plotting inverted mean values (green). The EPG (black) was measured simultaneously, showing (from left to right) typical spikes: E/E2 excitation, inhibitory P spikes, as well as R1 and R2 repolarization; eFRET signal is overlaid in red.

pharynx allowed us to generate an "optical EPG," recapitulating most of the characteristic features of the classical EPG. Simultaneous electrical and optical measurements enable optimal ΔF/F signal calibration.

Finally, neuronal activity was also measurable using QuasAr. We expected this to be difficult since *C. elegans* neurons often exhibit only small membrane-potential changes. Cholinergic neurons showed activity in line with the graded potentials previously described for these neurons (46). The locomotion interneuron RIM exhibited fast de- or hyperpolarizing events, possibly due to presynaptic input. In line with Ca^{2+} imaging, RIM voltage also showed slow fluctuations that could represent a bistable membrane potential, corresponding to forward and reverse locomotion states of this neuron, and which could result from the integration of many concomitant small inputs to RIM. Future work will use (optogenetic) activation or inhibition of neurons up- or downstream of RIM, to explore the circuit activity in an all-optical manner, in intact, possibly even freely moving animals.

The combination of voltage imaging in the infrared and blue-light stimulation of ChR2 enables all-optical electrophysiology approaches for *C. elegans*, and will greatly facilitate such measurements, bypassing complicated electrophysiological approaches (47). It should further enable analyzing mutants affecting neuromuscular junction function that are too small to allow dissection for patch-clamp electrophysiology. That voltage imaging is performed in intact animals is a distinct advantage over measurements in dissected animals, since the composition of extracellular and pipette solutions may alter the endogenous physiology. In sum, we compared a range of useful tools for all-optical interrogation of muscular tissues, cell ensembles, and neurons, in response to intrinsic activities, as well as optogenetically evoked neurotransmission, and provide guidelines for their use in *C. elegans*.

Materials and Methods

An extended Materials and Methods section is provided in *SI Appendix*.

***C. elegans* Culture and Transgenic Animals and Molecular Biology.** *C. elegans* culture and transgenic animals and molecular biology were all according to standard methods and are described in detail in *SI Appendix*.

Voltage and Ca^{2+} Imaging of Immobilized Animals. Information on animal preparation and imaging conditions, as well as microscope setup, are mostly standard procedures and explained in *SI Appendix*.

Animals were cultivated in the presence of ATR or respective ATR-analogs [final ATR concentration: 0.01 mM for ChR2 or ACR2 blue-light stimulation, 1 mM for imaging Arch(D95N) in pharynx, and 0.1 mM for imaging eFRET sensors]. APs were observed clearly only with 637-nm laser excitation, 180 mW/mm^2 (in pharynx), and 1.8 W/mm^2 for imaging of QuasAr and Archon in BWMs. For imaging, worms were immobilized with polystyrene beads. Imaging was performed on an inverted microscope (Zeiss Axio Observer Z1), equipped with 40× oil immersion objective (Zeiss EC Plan-NEOFLUAR 40×/N.A. 1.3, Oil DIC ∞/0.17), LED light sources (KSL 70, Rapp OptoElectronic) or monochromator (PolychromeV, Till Photonics) for photostimulation, a 637-nm laser (OBIS FP 637LX, Coherent) for excitation of voltage sensors, a galilean beam expander (BE02-05-A, Thorlabs), and an EMCCD Camera (Evolve 512 Delta, Photometrics). Voltage sensor fluorescence was imaged at 700 or 747 nm for ATR, and at 780 nm for DMAR. eFRET sensors were imaged with 545/30- or 472/30-nm excitation and 610/75- or 520/35-nm emission, respectively.

Processing and Automated Data Analysis of Pharyngeal Voltage and Pump Events. Processing and automated data analysis of pharyngeal voltage and pump events were done with an automated custom workflow in KNIME 3.6.2 (KNIME AG) (48), which was used to synchronize pump and voltage events

across animals by calling an R (R 3.5.1, The R Foundation for Statistical Computing; ref. 49) script to process each of the Excel tables (script accessible via https://open.ag.bmls.uni-frankfurt.de/s/qmLbijczkxAogEE).

Electrophysiology. Recordings were conducted from dissected BWM cells on the ventral side of the body anterior to the vulva as described earlier (47). EPG recordings and cut-head preparation were performed as described previously (38). Intracellular recordings were performed following a previously described protocol (41).

Software and Statistics. Software used was Knime 3.6.2 (KNIME AG), R 3.5.1 (The R Foundation for Statistical Computing). Statistics used were ANOVA with Bonferroni correction, after verification of normal distribution of the data.

Data and Reagent Availability. The original data, as fluorescence gray values of the relevant ROIs, can be found in Dataset S1. Plasmids have been deposited at Addgene, *C. elegans* strains are available on request.

ACKNOWLEDGMENTS. We thank Steven Flavell and Adam Cohen for reagents; and Sven Plath, Alexander Hirschhäuser, Heike Fettermann, Mona Hoeret, Regina Wagner, and Franziska Baumbach for expert technical assistance. DMAR and retinal analog VI were gifts from Lars Kattner (Endotherm). Some strains were provided by the *Caenorhabditis* Genetics Center, funded by NIH, Office of Research Infrastructure Programs Grant P40 OD010440. This work was funded by Goethe University and the Deutsche Forschungsgemeinschaft Grants SFB807-P11, GO1011/13-1, and EXC115 (Cluster of Excellence Frankfurt) (to A.G.); SCHU3177/1-1 (to C.S.); and by an IMPReS PhD stipend (to A.C.F.B.).

1. C. K. Kim, A. Adhikari, K. Deisseroth, Integration of optogenetics with complementary methodologies in systems neuroscience. *Nat. Rev. Neurosci.* **18**, 222–235 (2017).
2. T. Knöpfel, Genetically encoded optical indicators for the analysis of neuronal circuits. *Nat. Rev. Neurosci.* **13**, 687–700 (2012).
3. Y. Xu, P. Zou, A. E. Cohen, Voltage imaging with genetically encoded indicators. *Curr. Opin. Chem. Biol.* **39**, 1–10 (2017).
4. S. D. Antic, R. M. Empson, T. Knöpfel, Voltage imaging to understand connections and functions of neuronal circuits. *J. Neurophysiol.* **116**, 135–152 (2016).
5. M. Z. Lin, M. J. Schnitzer, Genetically encoded indicators of neuronal activity. *Nat. Neurosci.* **19**, 1142–1153 (2016).
6. J. H. Simpson, L. L. Looger, Functional imaging and optogenetics in *Drosophila*. *Genetics* **208**, 1291–1309 (2018).
7. J. R. Enterina, L. Wu, R. E. Campbell, Emerging fluorescent protein technologies. *Curr. Opin. Chem. Biol.* **27**, 10–17 (2015).
8. H. Dana *et al*., Sensitive red protein calcium indicators for imaging neural activity. *eLife* **5**, e12727 (2016).
9. J. Akerboom *et al*., Genetically encoded calcium indicators for multi-color neural activity imaging and combination with optogenetics. *Front. Mol. Neurosci.* **6**, 2 (2013).
10. T. W. Chen *et al*., Ultrasensitive fluorescent proteins for imaging neuronal activity. *Nature* **499**, 295–300 (2013).
11. Y. Gong, J. Z. Li, M. J. Schnitzer, Enhanced archaerhodopsin fluorescent protein voltage indicators. *PLoS One* **8**, e66959 (2013).
12. P. D. E. Williams *et al*., Serotonin disinhibits a *Caenorhabditis elegans* sensory neuron by suppressing Ca^{2+}-dependent negative feedback. *J. Neurosci.* **38**, 2069–2080 (2018).
13. K. D. Piatkevich *et al*., A robotic multidimensional directed evolution approach applied to fluorescent voltage reporters. *Nat. Chem. Biol.* **14**, 352–360 (2018).
14. Y. Gong, M. J. Wagner, J. Zhong Li, M. J. Schnitzer, Imaging neural spiking in brain tissue using FRET-opsin protein voltage sensors. *Nat. Commun.* **5**, 3674 (2014).
15. N. C. Flytzanis *et al*., Archaerhodopsin variants with enhanced voltage-sensitive fluorescence in mammalian and Caenorhabditis elegans neurons. *Nat. Commun.* **5**, 4894 (2014).
16. P. Zou *et al*., Bright and fast multicoloured voltage reporters via electrochromic FRET. *Nat. Commun.* **5**, 4625 (2014).
17. J. M. Kralj, A. D. Douglass, D. R. Hochbaum, D. Maclaurin, A. E. Cohen, Optical recording of action potentials in mammalian neurons using a microbial rhodopsin. *Nat. Methods* **9**, 90–95 (2011).
18. D. R. Hochbaum *et al*., All-optical electrophysiology in mammalian neurons using engineered microbial rhodopsins. *Nat. Methods* **11**, 825–833 (2014).
19. J. M. Kralj, D. R. Hochbaum, A. D. Douglass, A. E. Cohen, Electrical spiking in Escherichia coli probed with a fluorescent voltage-indicating protein. *Science* **333**, 345–348 (2011).
20. D. Maclaurin, V. Venkatachalam, H. Lee, A. E. Cohen, Mechanism of voltage-sensitive fluorescence in a microbial rhodopsin. *Proc. Natl. Acad. Sci. U.S.A.* **110**, 5939–5944 (2013).
21. Y. Gong *et al*., High-speed recording of neural spikes in awake mice and flies with a fluorescent voltage sensor. *Science* **350**, 1361–1366 (2015).
22. M. Kannan *et al*., Fast, in vivo voltage imaging using a red fluorescent indicator. *Nat. Methods* **15**, 1108–1116 (2018).
23. N. AzimiHashemi *et al*., Synthetic retinal analogues modify the spectral and kinetic characteristics of microbial rhodopsin optogenetic tools. *Nat. Commun.* **5**, 5810 (2014).
24. S. Gao, M. Zhen, Action potentials drive body wall muscle contractions in Caenorhabditis elegans. *Proc. Natl. Acad. Sci. U.S.A.* **108**, 2557–2562 (2011).
25. P. Liu *et al*., Genetic dissection of ion currents underlying all-or-none action potentials in C. elegans body-wall muscle cells. *J. Physiol.* **589**, 101–117 (2011).
26. O. Tolstenkov *et al*., Functionally asymmetric motor neurons contribute to coordinating locomotion of *Caenorhabditis elegans*. *eLife* **7**, e34997 (2018).
27. A. Bergs *et al*., Rhodopsin optogenetic toolbox v2.0 for light-sensitive excitation and inhibition in Caenorhabditis elegans. *PLoS One* **13**, e0191802 (2018).
28. E. G. Govorunova, O. A. Sineshchekov, R. Janz, X. Liu, J. L. Spudich, Neuroscience. Natural light-gated anion channels: A family of microbial rhodopsins for advanced optogenetics. *Science* **349**, 647–650 (2015).
29. T. Kawano *et al*., An imbalancing act: Gap junctions reduce the backward motor circuit activity to bias C. elegans for forward locomotion. *Neuron* **72**, 572–586 (2011).
30. B. J. Piggott, J. Liu, Z. Feng, S. A. Wescott, X. Z. S. Xu, The neural circuits and synaptic mechanisms underlying motor initiation in C. elegans. *Cell* **147**, 922–933 (2011).
31. V. Venkatachalam *et al*., Pan-neuronal imaging in roaming Caenorhabditis elegans. *Proc. Natl. Acad. Sci. U.S.A.* **113**, E1082–E1088 (2016).
32. Y. Kagawa-Nagamura, K. Gengyo-Ando, M. Ohkura, J. Nakai, Role of tyramine in calcium dynamics of GABAergic neurons and escape behavior in *Caenorhabditis elegans*. *Zoological Lett.* **4**, 19 (2018).
33. M. W. Davis, R. Fleischhauer, J. A. Dent, R. H. Joho, L. Avery, A mutation in the C. elegans EXP-2 potassium channel that alters feeding behavior. *Science* **286**, 2501–2504 (1999).
34. K. A. Steger, B. B. Shtonda, C. Thacker, T. P. Snutch, L. Avery, The C. elegans T-type calcium channel CCA-1 boosts neuromuscular transmission. *J. Exp. Biol.* **208**, 2191–2203 (2005).
35. C. J. Franks *et al*., Ionic basis of the resting membrane potential and action potential in the pharyngeal muscle of Caenorhabditis elegans. *J. Neurophysiol.* **87**, 954–961 (2002).
36. B. Shtonda, L. Avery, CCA-1, EGL-19 and EXP-2 currents shape action potentials in the Caenorhabditis elegans pharynx. *J. Exp. Biol.* **208**, 2177–2190 (2005).
37. R. Y. Lee, L. Lobel, M. Hengartner, H. R. Horvitz, L. Avery, Mutations in the alpha1 subunit of an L-type voltage-activated Ca2+ channel cause myotonia in Caenorhabditis elegans. *EMBO J.* **16**, 6066–6076 (1997).
38. C. Schüler, E. Fischer, L. Shaltiel, W. Steuer Costa, A. Gottschalk, Arrhythmogenic effects of mutated L-type Ca 2+-channels on an optogenetically paced muscular pump in Caenorhabditis elegans. *Sci. Rep.* **5**, 14427 (2015).
39. T. C. Kwok *et al*., A small-molecule screen in C. elegans yields a new calcium channel antagonist. *Nature* **441**, 91–95 (2006).
40. D. M. Raizen, L. Avery, Electrical activity and behavior in the pharynx of Caenorhabditis elegans. *Neuron* **12**, 483–495 (1994).
41. A. Cook, C. J. Franks, L. Holden-Dye, Electrophysiological recordings from the pharynx. *WormBook* **17**, 1–7 (2006).
42. L. Avery, D. Raizen, S. Lockery, Electrophysiological methods. *Methods Cell Biol.* **48**, 251–269 (1995).
43. M. W. Davis *et al*., Mutations in the Caenorhabditis elegans Na,K-ATPase alpha-subunit gene, eat-6, disrupt excitable cell function. *J. Neurosci.* **15**, 8408–8418 (1995).
44. K. A. Steger, L. Avery, The GAR-3 muscarinic receptor cooperates with calcium signals to regulate muscle contraction in the Caenorhabditis elegans pharynx. *Genetics* **167**, 633–643 (2004).
45. J. Dillon *et al*., AutoEPG: Software for the analysis of electrical activity in the microcircuit underpinning feeding behaviour of Caenorhabditis elegans. *PLoS One* **4**, e8482 (2009).
46. Q. Liu, G. Hollopeter, E. M. Jorgensen, Graded synaptic transmission at the Caenorhabditis elegans neuromuscular junction. *Proc. Natl. Acad. Sci. U.S.A.* **106**, 10823–10828 (2009).
47. J. F. Liewald *et al*., Optogenetic analysis of synaptic function. *Nat. Methods* **5**, 895–902 (2008).
48. M. Berthold *et al*., "KNIME: The Konstanz information miner" in *Data Analysis, Machine Learning and Applications*, C. Preisach, H. Burkhardt, L. Schmidt-Thieme, R. Decker, Eds. (Studies in Classification, Data Analysis, and Knowledge Organization, Springer, 2008), pp. 319–326.
49. R Core Team, R: A language and environment for statistical computing (Version 3.5.1, R Foundation for Statistical Computing, Vienna, Austria, 2014).